J Mater Sci (2008) 43:2602–2610
DOI 10.1007/s10853-008-2469-5

Creep rupture mechanisms of 5083-Al alloy under multiaxial stress states

Ho-Kyung Kim · Hyun-Jun Kim

Received: 31 March 2007 / Accepted: 14 January 2008 / Published online: 20 February 2008

Abstract The high-temperature rupture behavior of the 5083-Al alloy was tested to failure at 548 K under multiaxial stress states of uniaxial tension using smooth bar specimens, biaxial shearing using double shear bar specimens, and triaxial tension using notched bar specimens. Rupture times were compared for uniaxial, biaxial, and triaxial stress states with respect to the maximum principal stress, the von-Mises effective stress, and the principal facet stress. The results indicate that the von Mises effective and principal facet stresses show a good correlation for the investigated material. The success with two parameters implies that the creep rupture of the 5083-Al alloy is dominated by grain boundary cavitation that is constrained by the creep deformation of the surroundings. The experimental results reveal that the creep rupture of this alloy under the testing condition in the present study is controlled by cavitation coupled with the highly localized deformation process such as grain boundary sliding. The failure-mechanism control parameter for the notched triaxial tension specimens confirms that the effective stress primarily controls the rupture of the uniaxial and triaxial tension specimens. A theoretical prediction based on constrained cavity growth and continuous nucleation was found to be in agreement with the experimental rupture data within a factor of three.

H.-K. Kim (✉)
Department of Automotive Engineering, Seoul National University of Technology, 172 Kongnung-dong, Nowon-ku, Seoul 139-743, Korea
e-mail: kimhk@snut.ac.kr

H.-J. Kim
Graduate School, Seoul National University of Technology, 172 Kongnung-dong, Nowon-ku, Seoul 139-743, Korea

Introduction

Intergranular creep fractures of structural components at elevated temperatures have been studied extensively for more than 30 years [1]. These fractures frequently occur as a result of by the nucleation, growth, and coalescence of intergranular cavities. This mode of failure has been studied primarily under uniaxial stresses. However, uniaxial stress experiments do not provide sufficient information to predict the creep rupture lifetime under a multiaxial stress state. Most components in service are subjected to a multiaxial stress system, as multiaxial stress states are produced at notches and other geometric irregularities even under basic remote uniaxial loading. An incorrectly assumed multiaxial stress rupture criterion can result in an incorrect design.

Several methods have been proposed for correlating creep life data for different multiaxial stress states [2–5]. Most of these methods are based on continuum mechanics arguments, while others are based on particular physical mechanisms that can influence grain boundary cavitation. Hayhurst [2] has shown that for a smooth cylindrical specimen subjected to uniaxial tension, the rupture lifetime at a given temperature can be expressed as:

$$t_f = M\sigma^{-m} \tag{1}$$

where σ is the uniaxial stress and M and m are parameters that characterize the evolution of damage at the temperature in equation. It has been suggested that an equation of this form can be used to describe multiaxial behavior. It is generally assumed that the stress term in Eq. 1 can be replaced by a representative stress term, σ_{rep}, as follows:

$$t_r = M\sigma_{\text{rep}}^{-m} \tag{2}$$

The representative stress, σ_{rep}, is defined as the stress applied in a uniaxial smooth bar specimen with the same lifetime as multiaxial specimens. Several parameters that contain adjustable constants have been proposed to correlate rupture times for multiaxial stress states [6, 7]. However, the present work only considers the non-adjustable representative stress parameters of the maximum principal stress σ_{MPS}, the von-Mises effective stress σ_e and the principal facet stress σ_{PFS}, as proposed by Nix et al. [8]. The principal facet stress is given by

$$\sigma_{PFS} = 2.24\sigma_1 - 0.62(\sigma_2 + \sigma_3) \quad (3)$$

where $\sigma_1 > \sigma_2 > \sigma_3$ are the principal stresses. The application of these parameters to predict the lifetime of a specimen can be utilized for the determination of the mechanisms that control creep fracture in samples. In an earlier study [8], the maximum principal stress correlates well with the rupture time when failure occurs primarily by unconstrained cavity growth where the cavity growth rate is governed only by tensile stress driving the diffusive cavity growth process. The effective stress correlates well when failure occurs primarily by constrained cavity growth where the cavity growth rate is governed only by shear stress or when microstructural strain softening occurs during creep. The principal facet stress correlates well when stress distribution after grain boundary sliding can significantly enhance the creep damage on the transverse facets that facilitates high-temperature fractures. Thus, application of these parameters in lifetime predictions may be utilized for determination of the mechanisms that control creep fracture in samples.

Thus, the motivation of the present study is to investigate the creep rupture behavior of the 5083-Al alloy under different stress states. Attention will be focused on the validity of the aforementioned mechanistic criteria that describes creep rupture in this alloy. In addition, the proportion of the governing stress state leading to a rupture in this alloy is evaluated under a multiaxial stress state.

Experimental procedures

The material used in this investigation is the 5083-Al alloy having an average equiaxed grain size of 205 μm. The nominal composition of this alloy is (in wt.%) 4.4 Mg, 0.7 Mn, 1.15 Cr, with the balanace Al. Samples were solid solutionized at 723 K for 6 h and subsequently cooled in air to room temperature. All creep rupture tests were conducted in air using a constant load machine. The specimens were tested under a maximum tensile stress ranging from 11.7 to 75 MPa at 548 ± 1 K. Three types of specimens, each corresponding to different stress states, were utilized in this investigation (Table 1). For the uniaxial stress state, smooth cylindrical specimens were used (Fig. 1a). A tensile load was applied at the ends of the specimen for the uniaxial stress.

Table 1 Stress analysis and stress parameters for the specimen geometries

		Uniaxial tension	Double shear	Triaxial tension
Stress analysis	σ_{norm}	P/A_{min}	$0.78\ P/2A_{min}$	P/A_{norm}
	σ_1	σ_{norm}	σ_{norm}	$2.7\sigma_{norm}$
	σ_2	0	0	$0.33\sigma_1$
	σ_3	0	$-\sigma_{norm}$	$0.33\sigma_1$
Stress parameter	σ_{MPS}	σ_{norm}	σ_{norm}	$2.7\sigma_{norm}$
	σ_e	σ_{norm}	$1.73\sigma_{norm}$	$1.81\sigma_{norm}$
	σ_{PFS}	$2.24\sigma_{norm}$	$2.86\sigma_{norm}$	$4.94\sigma_{norm}$

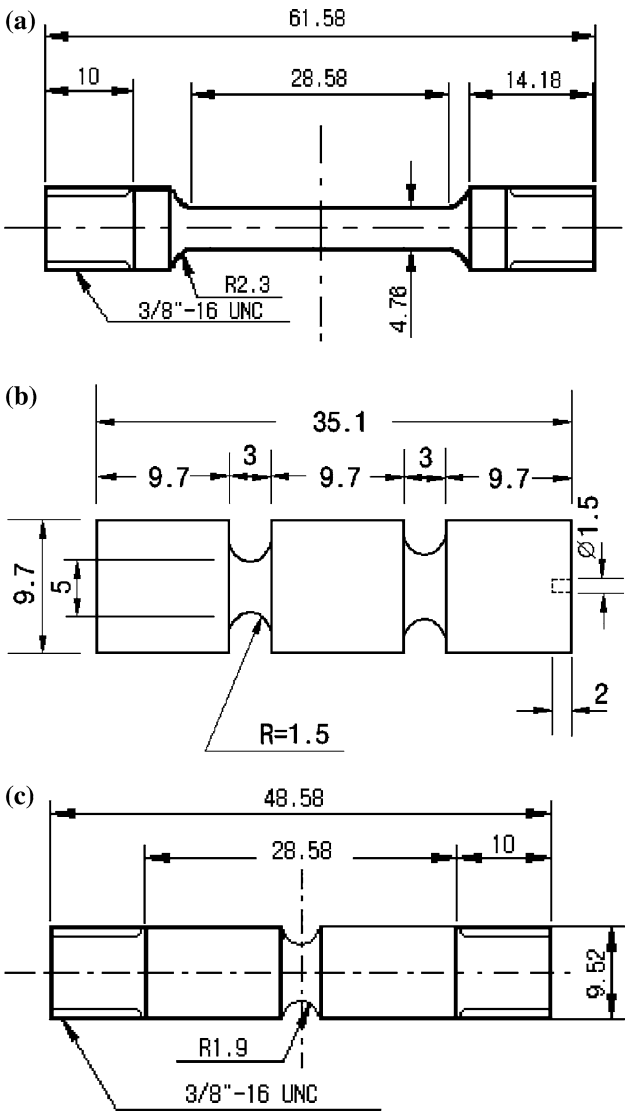

Fig. 1 The specimen geometries and dimensions used the present study: (**a**) uniaxial tension, (**b**) biaxial double shear and triaxial tension stresses

For the biaxial stress state, double shear geometry specimens were used. The double shear system is capable of inducing simple shear to moderate strains. The conventional double shear geometry is characterized by the presence of sharp corners at the ends of the gage section. In order to avoid the development of cracks at the sharp corners in the gage section, the corners were replaced with round notches, as shown in Fig. 1b. It is assumed that stress concentrations in the gage section are relaxed early in the life of the specimen, and that the steady-state deformation rate should be related to the mean shear stress over the total gage section rather than that at the minimum cross section. The mean shear stress $\bar{\tau}$ for the double shear geometry is given by

$$\bar{\tau} = \frac{P}{\pi \bar{r}^2} \tag{4}$$

where $\bar{r}$ is the mean specimen radius and P is the shear load imposed on each gage section. The mean specimen radius $\bar{r}$ is determined by

$$\bar{r} = \frac{\int_0^R r_s dx}{\int_0^{2R} dx} \tag{5}$$

where r_s is the radius in the shoulders (Fig. 2), and x is the position along the axis of the specimen. The radius in the shoulder is given by

$$r_s = R_{\min} + R - \sqrt{R^2 - x^2} \tag{6}$$

Substituting Eq. 6 into Eq. 5 and solving for the integral terms result in

$$\bar{r} = R_{\min} + R - \frac{\pi R}{4} \tag{7}$$

The values of R and $R_{\min}$ for the current specimen are 1.5 and 2.5 mm, respectively. By substituting $0.6R_{\min}$ for R in Eq. 7, $\bar{r} = 1.13R_{\min}$ is obtained. Finally, the ratio of mean shear stress divided by shear stress at the minimum cross section, $\bar{\tau}/\tau$ is given by

$$\frac{\bar{\tau}}{\tau} = \left(\frac{R_{\min}}{\bar{r}}\right)^2 = 0.78 \tag{8}$$

The modified round notch double shear specimen has been verified in several works through both experimental and numerical methods [9, 10].

For triaxial stress conditions, a Bridgman cylindrical specimen with a circular notch in the center was used, as shown in Fig. 1c. Finite element calculations of the steady-state multiaxial stress distributions for this notched bar geometry were reported by Hayhurst et al. [3]. Their results indicate that once steady-state conditions are reached, the ratio of the maximum principal stress, σ_1, to the remotely applied stress is 2.7 for the remaining life of the specimen. Their results also indicate that the ratio of the maximum principal stress over the effective stress is equal to 1.49 and $\sigma_T = \sigma_2 = \sigma_3 = 0.33\sigma_1$, where σ_T is the transverse stress acting at the notch center. The test conditions for the multiaxial stress states are summarized in Table 2.

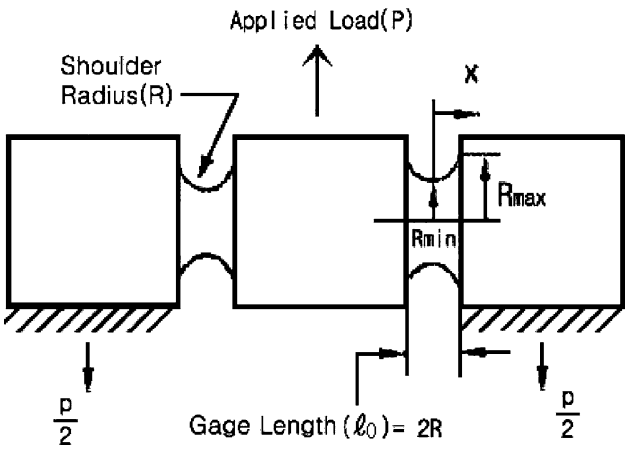

Fig. 2 Geometry and loading configuration of the modified circular notch double specimen

Results and discussion

The high-temperature rupture data for the 5083-Al alloy are shown in Fig. 3 as the maximum principal stress plotted against the logarithm of the rupture time. The data indicate that this stress term is not successful in bringing the data together onto a single curve. The maximum principal stress should be valid when cavitation damage is diffusive by nature and unconstrained by creep deformation [11]. Thus, it appears from these results that the cavitation damage is not dominant in determining the life of the specimens, or that the cavitation damage is constrained by creep deformation. The biaxial data lie below and the triaxial data above the uniaxial tension data. Essentially, for the same maximum principal stress, a biaxial specimen fails sooner than a uniaxial specimen does, while the failure of a triaxial specimen takes longer than the failure of a uniaxial specimen. This implies that a triaxial specimen is stronger than a uniaxial specimen, which implies that there is a notch-strengthening effect.

The notch-strengthening effect has been observed in high-temperature ruptures of other alloys [8, 12]. The notch-strengthening effect can be explained partly by the suppression of cavity growth rate in the present notched specimen. Most of the cavities are located on the grain boundary and the normal stress to the boundary governs cavity growth, driving the cavity-absorbing vacancies on the boundary. Moreover, during grain boundary sliding in an equiaxed grain, the shear stresses on the inclined

Table 2 Summary of the multiaxial creep rupture test data of the 5083-Al alloy at 548 K

Specimen type	σ_1 (MPa)	σ_e (MPa)	σ_{PFS} (MPa)	T_r (sec)	Minimum strain Rate (1/s)	Rupture strain, ε_f (%)
Uniaxial	20.0	20.0	44.8	651,600	9.1×10^{-8}	16.1
Uniaxial	30.0	30.0	67.2	145,500	8.0×10^{-7}	33.2
Uniaxial	40.0	40.0	89.6	44,040	2.2×10^{-6}	18.7
Uniaxial	60.0	60.0	134.4	3,720	3.1×10^{-5}	29.1
Double shear	11.7	20.2	33.5	3,188,500	–	–
Double shear	15	26.0	42.9	622,500	–	–
Double shear	20	34.6	57.2	144,500	–	–
Double shear	25	43.3	71.5	34,560	–	–
Double shear	30	52.0	85.8	19,560	–	–
Double shear	50	86.6	143	3,540	–	–
Triaxial tension	25	16.8	45.8	2,494,800	–	–
Triaxial tension	30	20.1	54.9	478,860	–	–
Triaxial tension	35	23.5	64.1	412,980	–	–
Triaxial tension	50	33.6	91.5	60,600	–	–
Triaxial tension	60	40.3	109.8	25,620	–	–
Triaxial tension	75	50.3	137.3	6,960	–	–

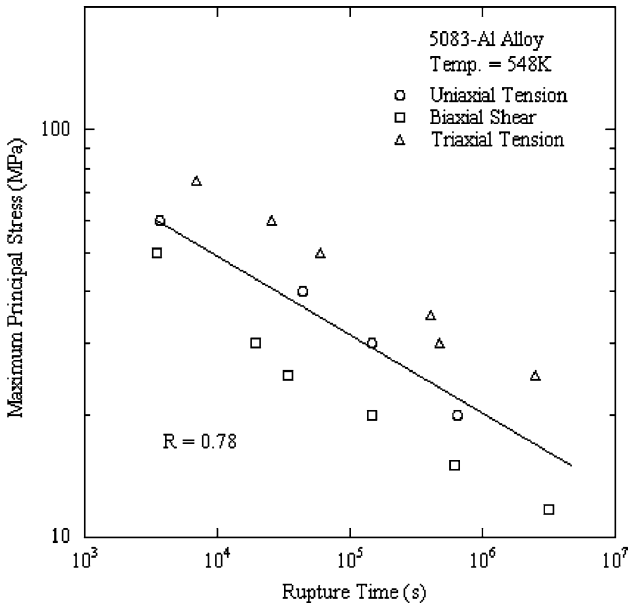

Fig. 3 Maximum principal stress against the rupture time for 5083-Al specimens tested at 548 K

boundaries are relieved, giving rise to a redistribution of normal stresses. Finally, the normal tensile stress on the boundary is amplified, resulting in accelerating cavitation. The transverse tensile stress acting on the boundary prevents the grain boundary sliding, which results in a decrease of the normal stress and thus a notch-strengthening effect.

It appears that if the two transverse stresses are compressively imposed, instead of tensile stresses, they would enhance the grain boundary sliding and finally reduce the rupture time. It is conceivable that for biaxial shear stress tests, a compressive transverse stress perpendicular to the maximum tensile stress enhances the grain boundary sliding. This causes rupture time of the biaxial shear specimen to be shorter than that of the uniaxial tension specimen at the same maximum principal stress. This concept can be tested through the application of principal facet stress, as shown in Fig. 4. For example, in a triaxial stress state, if the transverse stress is positive, the final principal facet stress will be reduced, according to Eq. 3. This causes a reduction of the cavity growth rate. In addition, for the biaxial shear stress state, one stress component is tensile

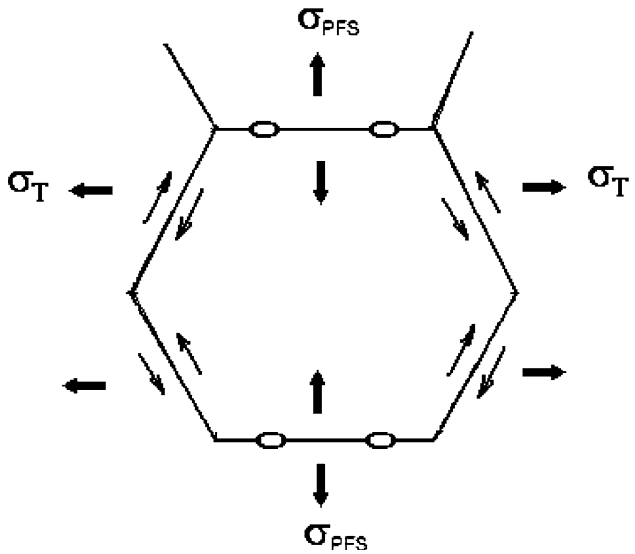

Fig. 4 Reduction of the principal facet stress due to suppressing grain boundary sliding by positive transverse tensile stresses

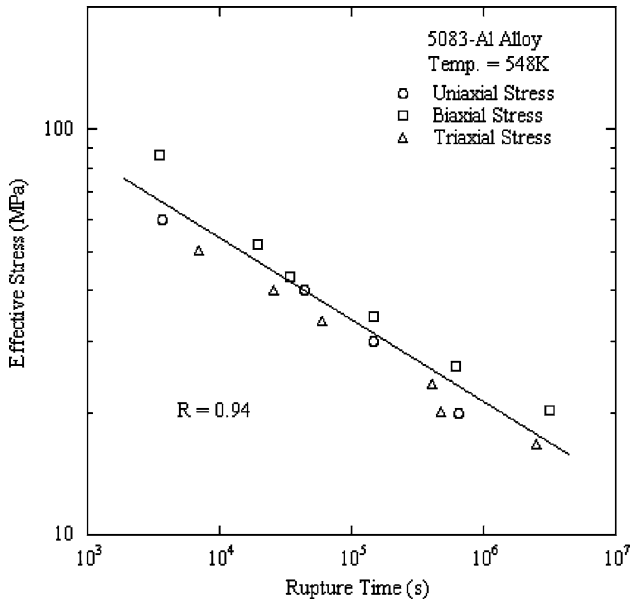

Fig. 5 Effective stress against the rupture time for the 5083-Al specimens tested at 548 K

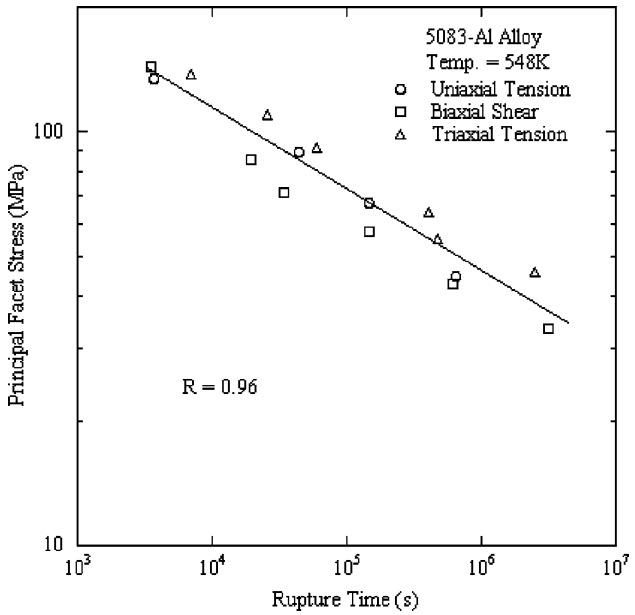

Fig. 6 Principal facet stress against the rupture time for the 5083-Al specimens tested at 548 K

and the other stress is compressive with the same magnitude. The negative stress component in the second term of Eq. 3 increases the facet stress, which enhances the cavity growth rate.

The von-Mises effective stress is plotted against the rupture time for the 5083-Al alloy in Fig. 5. This figure shows that the effective stress is successful in bringing the rupture times for different stress states into coincidence ($R \approx 0.94$). Thus, it appears from these results that creep deformation processes may be dominant in determining the life of the specimens. The principal facet stress was determined for the data shown in Figs. 3 and 5. It is plotted against the rupture time in Fig. 6. It is evident that the principal facet stress correlates the rupture time for the 5083-Al alloy ($R \approx 0.96$), bringing the data onto a single curve for the entire range of stresses, similar to the von-Mises effective stress. The success of the principal facet stress indicates that either grain boundary sliding or softening processes along the inclined boundaries could be a significant component of the rupture process according to the approach by Nix et al. [8].

The success of two stress parameters, von Mises and principal facet stresses, to correlate the rupture time under multiaxial stresses implies that during creep rupture, different mechanisms occur in a coupled manner, with each being dominant for a certain fraction of the creep life. In other words, creep rupture of this alloy under the testing condition is controlled by the cavitation coupled with a highly localized deformation process such as grain boundary sliding. It is also conceivable that creep deformation controls the highly localized deformation modes. Conclusively, it suggests that creep rupture in the 5083-Al alloy is dominated by grain boundary cavitation that is constrained by the creep deformation of the surroundings.

While attempting to identify mechanisms that control the creep rupture, it is helpful to consider the damage tolerance parameter λ, defined as

$$\lambda = \frac{\varepsilon_f}{\dot{\varepsilon} t_r} \tag{9}$$

where ε_f is the rupture strain, $\dot{\varepsilon}$ is the minimum strain rate, and t_r is the time to rupture. Dyson and Leckie [13] noted that alloys that fail by diffusive cavitation and exhibit very little strain softening generally have λ values that lie between 1 and 2.5. They also suggest that microstructural softening can be a dominant damage mechanism when λ takes on larger values (commonly greater than 5). At intermediate levels, the likelihood of an interaction between the two mechanisms exists. Strain against the product of the minimum strain rate and time, $\dot{\varepsilon} \cdot t_r$ is plotted in Fig. 7 for a 5083-Al specimen tested at 20 MPa under uniaxial tension. Reference lines with slopes representing two values of λ are also shown on this plot. The rupture data in this figure correspond to λ values that are close to 2.72, suggesting that significant microstructural softening did not occur according to the approach by Dyson and Leckie [13]. The values of λ generally vary with the applied stress. This can be illustrated in the plot of λ against the maximum principal stress shown in Fig. 8. The dashed line region represents the cavitation-controlled region. The data in this figure indicate that the λ values range from 1.9 to a maximum of approximately 2.8. This

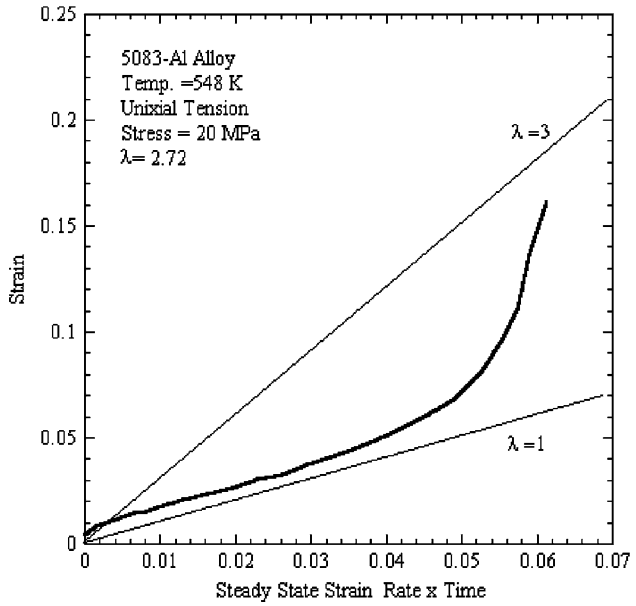

Fig. 7 Strain against time multiplied by the steady-state strain rate for the 5083-Al specimen at 80 MPa

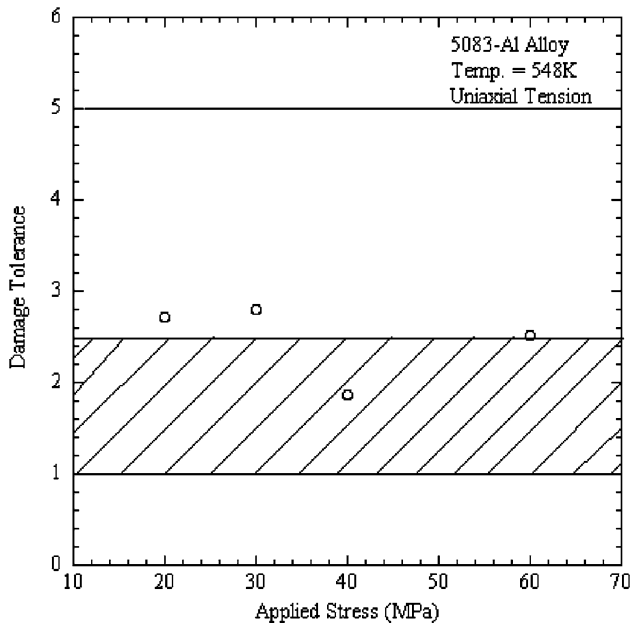

Fig. 8 Damage tolerance (λ) against stress for specimens tested in the present investigation under uniaxial tension

suggests that the creep fracture of the present specimens predominately fail by creep cavitation rather than by bulk microsoftening. The low values of λ and the failure of the maximum principal stress to correlate the rupture time under multiaxial stresses imply that creep rupture of the 5083-Al alloy is dominated by constrained cavitation. This implication is consistent with the results of the success of the von Mises and principal facet stresses to correlate the

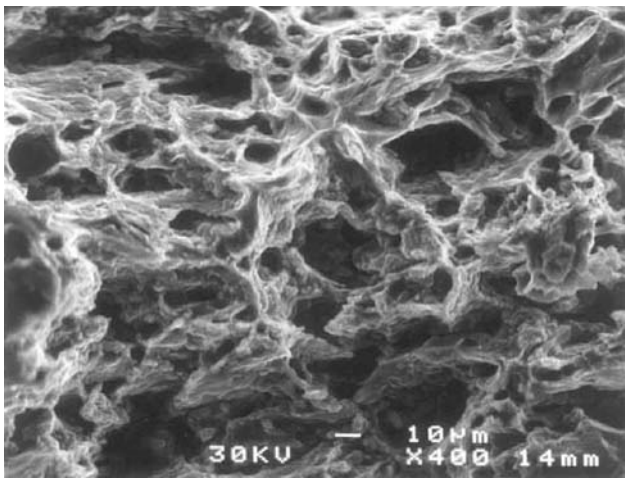

Fig. 9 SEM micrographs of the rupture surface of a uniaxial specimen at $\sigma_1 = 30$ MPa

rupture time. In addition, these results are consistent with fractographic observations of relatively deep dimples representing ductile rupture processes. An SEM micrograph of the rupture surface of a uniaxial specimen tested at $\sigma_1 = 30$ MPa is shown in Fig. 9. This figure shows that this alloy finally fails in a ductile manner, as characterized by the appearance (dimples with sharp ridges) of the rupture surfaces. The dimples indicate that considerable plastic deformation took place during the final stage of rupture. Sharp ridges are typically observed on the rupture surfaces of specimens that fail by constrained cavitation corresponding to regions that contain few intergranular cavities [14]. These regions, which constrain the cavity growth on the heavily cavitated grain boundaries before failure, must eventually rupture by extensive localized necking resulting in sharp ridges on the rupture surfaces.

When multiaxial stress rupture behavior is determined by a combination of the maximum principal stress and the effective stress, it is possible to evaluate the proportion of the governing stress state affecting the rupture of the materials under a multiaxial stress state. The relationship considered in this analysis was from Cane [15]. It is expressed as:

$$t_r = M\sigma_1^{-\gamma}\sigma_e^{\gamma-m} \tag{10}$$

where γ is the principal stress exponent of rupture and m is the slope of the uniaxial stress rupture life plot. The representative rupture stress for this criterion is then given by

$$\sigma_{rep} = \sigma_1^{\gamma/m}\sigma_e^{\,(m-\gamma)/m} \tag{11}$$

From Eqs. 1 and 11, this can be represented in the form

$$\log[t_{\text{mult}}(\sigma_e)/t_{\text{uni}}(\sigma_e)] = -\gamma \log(\sigma_1/\sigma_e) \tag{12}$$

where $t_{\text{mult}}(\sigma_e)/t_{\text{uni}}(\sigma_e)$ is the ratio of the rupture lifetime of multiaxial specimens to the rupture lifetime of a uniaxial

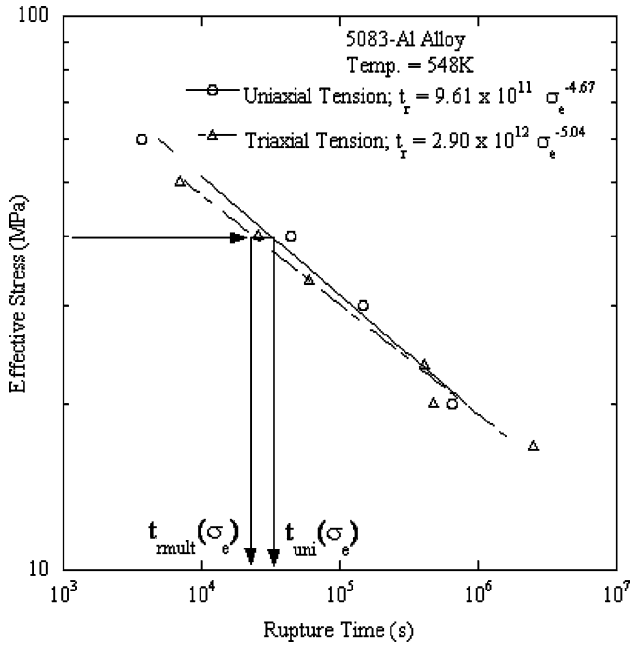

Fig. 10 Evaluation of normailized rupture time at the same effective stress

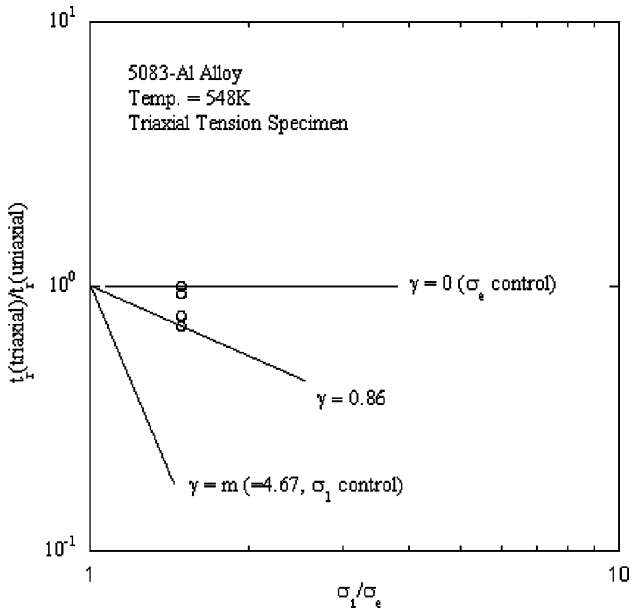

Fig. 11 Evaluation of γ of the triaxial tension specimens at 548 K

specimen at the same effective stress, as shown in Fig. 10. From the relationship between $t_{mult}(\sigma_e)/t_{uni}(\sigma_e)$ and (σ_1/σ_e), the principal stress exponent of the rupture, γ, can be determined from the slope of the log (rupture lifetime under multiaxial stress / rupture lifetime of a smooth bar under the same effective stress, σ_e) versus the log (σ_1/σ_e) data. A failure-mechanism control parameter can be defined as γ/m [16]. When γ/m is near or equal to 0, the rupture process of the material is mainly governed by the effective stress. If γ/m is close to or equal to 1, the maximum principal stress governs the multiaxial stress rupture lifetime. For $0 < \gamma/m < 1$, a combination of the effective stress and the maximum principal stress governs the rupture lifetime. The applicability of this model to the multiaxial stress rupture criterion for 2.25Cr1Mo steel was assessed previously in Kwon et al. [16].

In attempting to investigate the value of the failure-mechanism control parameter and its validity for the 5083-Al alloy, the stress- and temperature-dependent constant m and M in Eq. 1 were determined from the uniaxial creep rupture test data of the 5083-Al alloy. The constants m and M were evaluated by taking the slope of the uniaxial stress versus the rupture lifetime plot, as shown in Fig. 10. The constants m and M for the 5083-Al alloy at 548 K were determined as 4.67 and 9.61×10^{11}, respectively. The values of γ for the notched triaxial tension specimens were evaluated. Figure 11 illustrates the diagrammatical relationship between the normalized notch rupture lifetime and the ratio of the maximum principal stress to effective stress (=1.49) for triaxial and uniaxial specimens of the 5083-Al alloy. The values of γ differ depending on the normalized rupture lifetime at the same effective stress. The failure-mechanism control parameter defined as γ/m was evaluated for the 5083-Al alloy. The mixed failure stress control system in the notched triaxial tension specimens is schematically depicted in Fig. 12 in terms of the proportion percentage of each control parameter. The proportion of the maximum principal stress control is represented by the value of γ/m, while that of the effective stress control is the value of $(1-\ \gamma/m)$. This figure confirms that the effective stress primarily controls the rupture of the uniaxial and triaxial tension specimens of the 5083-Al alloy under the testing conditions. This fact is evident from Fig. 3, which shows that the maximum principal stress does not correlate the rupture times of both types of specimens, and from Fig. 5, which shows that the effective stress correlates the rupture time. In addition, Fig. 12 shows that the portion of the maximum principal stress slightly increases as the effective stress increases.

The values of γ for the biaxial double shear specimens were also evaluated at the ratio of the maximum principal stress to the effective stress (=0.58) for the specimens. The values of γ/m were found to be nearly zero for all of the specimens, suggesting that only the effective stress controls the rupture of the double shear specimens under the testing conditions. From the above results, it can be deduced that the rupture of uniaxial, biaxial, and triaxial tension specimens is primarily controlled by the effective stresses. This fact can be demonstrated from Fig. 5, which shows the

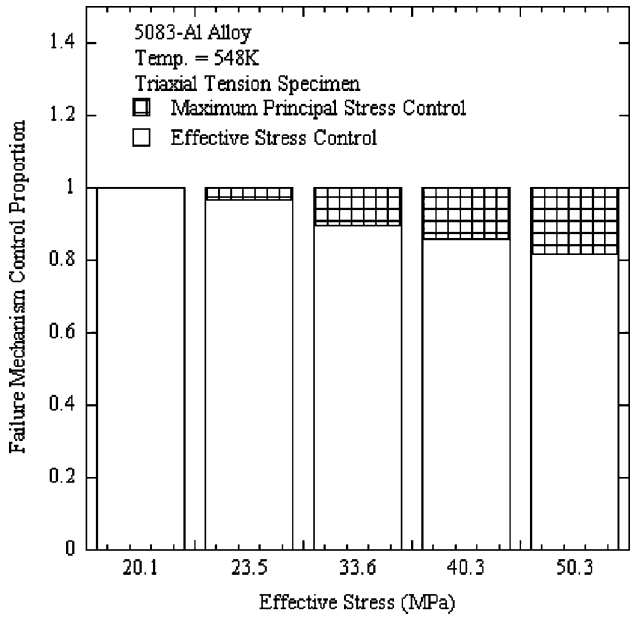

Fig. 12 Proportion of the governing multiaxial stress criterion for the triaxial tension. specimen of 5083-Al alloy

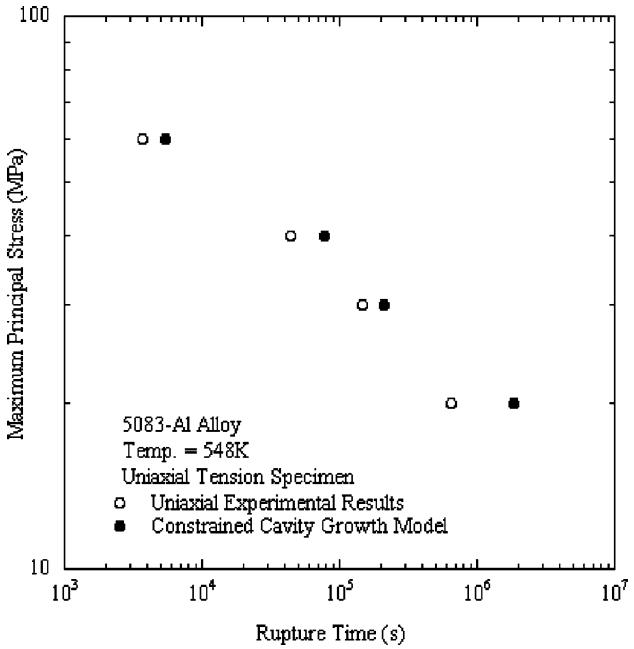

Fig. 13 Experimental and predicted rupture time values plotted against maximum principal stress for the 5083-Al alloy

correlation of effective stress to all the rupture lifetimes of the uniaxial, double shear, and triaxial tension specimens, as the effective stress controls the rupture of the uniaxial, biaxial, and triaxial tension specimens.

A theoretical model was applied for the prediction of the creep rupture lifetimes for the 5083-Al alloy. In an effort to compare the present experimental results with theoretical predictions, cavity nucleation and growth were considered as the controlling mechanisms for determining the life of the specimens. For the 5083-Al alloy, a model based on constrained cavity growth and continuous nucleation [14] was applied. For the constrained cavity growth with continuous nucleation under uniaxial tension, Ridel [1] proposed that the time to cavity coalescence on an isolated boundary facet is given by

$$t_r = \left(\frac{3\pi(1+3/n)}{J^*}\right)^{1/3}\left(\frac{h(\psi)}{\bar{\varepsilon}d}\right)^{2/3}\frac{\omega_f}{2.71} \tag{13}$$

Here, $h(\psi)$ is a geometric factor of the axisymmetric cavity, ω_f is the cavitated area fraction at the rupture, J^* is the cavity nucleation rate, d is grain boundary facet length, and n is the stress exponent. Introducing the cavity spacing at coalescence, $\lambda = (J^* t_r)^{-0.5}$ into the above equation gives

$$t_r = 0.69(1+3/n)^{1/2}\omega_f^{3/2}\left(\frac{h(\psi)\lambda}{\bar{\varepsilon}d}\right) \tag{14}$$

Here, the nucleation value of ω_f is somewhat arbitrary and was chosen as $\pi/4$, as regularly spaced round cavities touch each other if the cavitated area fraction of the grain boundaries with orientations between 60° and 90° to the tensile axis becomes $\pi/4$ [1]. The value of $h(\Phi)$ was determined to be 0.61 [1]. The value of d is assumed to be half of the grain size, or 102.5 μm. A constant strain to failure is given by $\varepsilon_f = \pi\lambda/6d_g$, where d_g is the grain size and λ is the cavity spacing. The average cavity spacing λ was determined to be 45.9 μm after averaging the strain-to-failure values at four different stresses (Table 2). The stress exponent n was determined to be 5.2. Experimental and predicted rupture time values are plotted as a function of the maximum principal stress in Fig. 13 for the 5083-Al alloy. It can be seen in this plot that the theoretical prediction was found to be in agreement with the experimental rupture data within a factor of three. These results indicate that the rupture process in this alloy is dominated by cavity nucleation and growth on the grain boundaries. The overall agreement of the model predictions with the experimental data indicates that constrained cavity growth on the transverse grain boundary is a critical mechanism in the rupture process.

Conclusions

High-temperature rupture data for 5083-Al alloy specimens under multiaxial stress states at 548 K were compared with respect to three different mechanistic parameters: the maximum principal stress, the von-Mises

effective stress, and the principal facet stress. The results indicate that the von Mises effective and principal facet stresses give a good correlation for the material investigated. The success of the two parameters implies that creep ruptures in the 5083-Al alloy are dominated by grain boundary cavitation that is constrained by the creep deformation of the surroundings. This implication is consistent with the results of the low values of λ and the failure of the maximum principal stress to correlate the rupture time under multiaxial stresses. The failure-mechanism control parameter defined as γ/m for the notched triaxial tension specimens was evaluated. The parameter confirms that the effective stress primarily controls the rupture of the uniaxial and triaxial tension specimens of the alloy under the testing conditions. A theoretical model based on constrained cavity growth and continuous nucleation was applied for the prediction of the creep rupture lifetimes for the 5083-Al alloy. The theoretical prediction was found to be in good agreement with the experimental rupture data within a factor of three.

References

1. Riedel H (1987) Fracture at high temperatures. Springer, Berlin
2. Hayhurst DR (1972) J Mech Phys Solids 20:381
3. Hayhurst DR, Leckie FA, Henderson JT (1977) Int J Mech Sci 19:147
4. Kim HK, Mohamed FA, Earthman JC (1991) Met Trans A 22:2629
5. Henderson J (1979) Trans ASME 101:356
6. Huddleston RL (1985) J Press Vessel Tech 107:421
7. Cane BJ (1982) In: Advances in fracture research (Fracture 81), vol 3. Pergamon Press, Oxford, United Kingdom, p 1285
8. Nix WD, Earthman JC, Eggeler G, Ilschner B (1989) Acta Metall 37:1067
9. Jonson NL, Earthman JC (1994) J Test Eval 22:111
10. Kim HK, Mohamed FA, Earthman JC (1992) J Test Eval 19:93
11. Cocks F, Ashby MF (1982) Prog Mater Sci 27:265
12. El-Nasr A, Mohamed FA, Earthman JC (1996) Mater Sci Eng A 214:33
13. Dyson BF, Leckie FA (1988) Mater Sci Eng A 103:111
14. Dyson BF (1976) Mater Sci 10:349
15. Cane BJ (1979) 3rd international conference on mechanical behavior of metals, vol 2, Pergamon Press, Cambridge, p 173
16. Kwon O, Thomas CW, Knowles D (2004) Int J Press Ves Pip 81:535